Supporting Information for

A quantitative connection of experimental and simulated folding landscapes by vibrational spectroscopy

Caitlin M. Davis, Laura Zanetti-Polzi, Martin Gruebele, Andrea Amadei, R. Brian Dyer, and Isabella Daidone

1. Difference spectra generated by subtracting the FTIR spectrum of GTT35 WW domain at 9 °C from higher temperature spectra has no isosbestic point, confirming that folding of GTT35 is non-two-state. The FTIR spectroscopy methodology is given in the experimental section of the full paper.

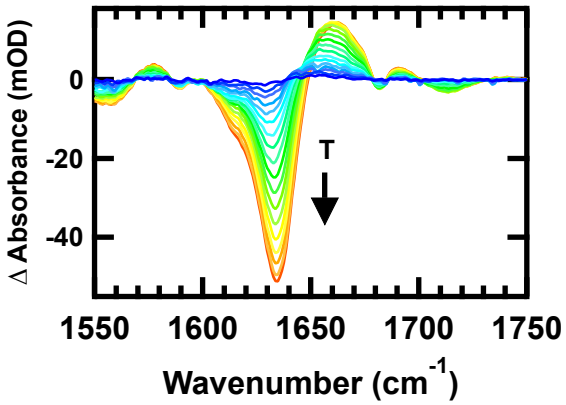

Figure S1. Temperature dependent FTIR spectra of 1 mM GTT35 WW domain in 20 mM potassium phosphate buffer pH 7. The temperatures of the individual traces varied between 9 and 88 °C in 5 °C intervals. The difference spectra are obtained by subtracting the spectrum of GTT35 at 9 °C from the spectra at higher temperatures.

2. An SVD analysis of the temperature dependent FTIR spectra requires four components to capture 80% of the variance in the temperature-dependent spectra. The FTIR spectroscopy methodology is given in the experimental section of the full paper. Singular value decomposition (SVD) was used to determine the number of spectral components required to describe the temperature dependence of the protein FTIR spectra.[1] The SVD and global fit methods have been described previously.[2] The temperature dependent data was used to construct a data matrix, A, where each column represents the spectra of interest at a specific temperature. SVD analysis of the data results in three matrices, $A=USV^T$, where U, S, and V^T are matrices containing the basis spectra, singular values and temperature evolution of the basis spectra, respectively. Basis spectra containing only noise were identified by their singular values and eliminated from the set of basis spectra. Four basis spectra were necessary to reconstruct the original data matrix A (Figure S2). The first component has a spectral shape similar to the amide I envelope. The spectral signature of the second component agrees well with the difference spectra for the low-temperature transition, and the spectral signature of the third component agrees well with the difference spectra of the high-temperature transition. This analysis also identifies a fourth component that contains additional changes in the β-sheets (1634 and 1680 cm^{-1}) and turn (1713 cm^{-1}).

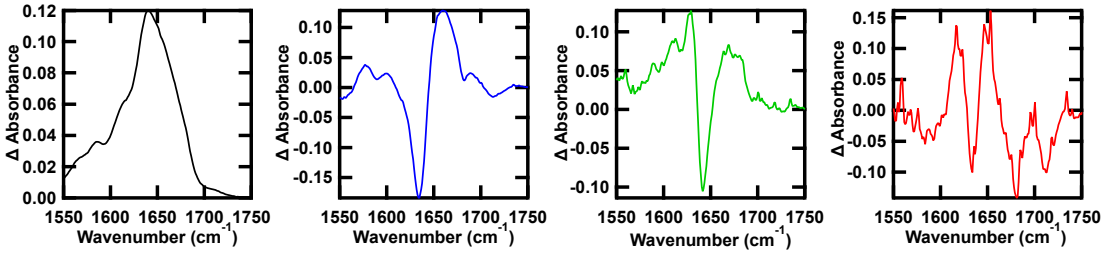

Figure S2. The spectral components determined from a SVD of the temperature-dependent GTT35 FTIR difference spectra. Component 1 is black, component 2 is blue, component 3 is green, and component 4 is red.

A global fit to a four-state model was used to determine the temperature dependence of the four spectral components (Figure S3). The temperature dependence of the four spectral components was fit by a mathematical model that consists of one sigmoidal transition for each of the three temperature-dependent spectral components:

$$f(T)_1 = w_{11} * \left(b_1 + \frac{m_1}{1+exp\left(\frac{(T_{m_1}-T)}{\Delta_1}\right)} \right) + w_{12} * \left(b_2 + \frac{m_2}{1+exp\left(\frac{(T_{m_2}-T)}{\Delta_2}\right)} \right) + \cdots$$

$$f(T)_2 = w_{21} * \left(b_1 + \frac{m_1}{1+exp\left(\frac{(T_{m_1}-T)}{\Delta_1}\right)} \right) + w_{22} * \left(b_2 + \frac{m_2}{1+exp\left(\frac{(T_{m_2}-T)}{\Delta_2}\right)} \right) + \cdots \quad \text{(S1)},$$

$$\vdots$$

where w is the weight of the sigmoidal transition found in each spectral component, and Tm and Δ represent the midpoint and width of each transition. The SVD analysis and data fitting was performed in IGOR PRO.

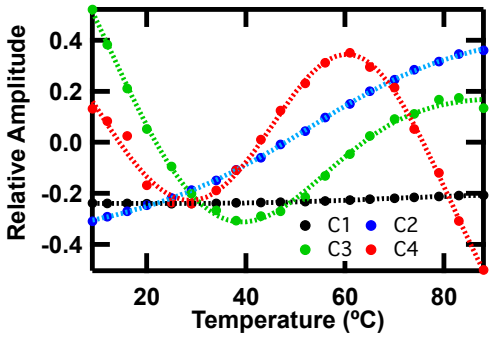

Figure S3. SVD analysis of the temperature-dependent FTIR spectra of GTT35. The temperature-dependent amplitude of the four principle components (basis FTIR spectra) is shown: C1 (black), C2 (blue), C3 (green), C4 (red). The data are globally fit to a four-state model (Equation S1).

The four basis spectra (Figure S2) capture 80% of the variance in the temperature-dependent FTIR spectra. The remaining spectral components have small amplitudes and represent noise in the data. The first component (C1) is invariant over the entire temperature range (Figure S3) and represents an average IR spectrum. There are three temperature-dependent components (Figure S3), C2, C3, and C4, which supports a folding model with at least four states. Each of the four states contributes to components C1-C4. A global fit determined three transition temperatures among the four states in the model: 16 ± 4 °C, 52 ± 16 °C, and 69 ± 14 °C. The large fitting uncertainty in the two higher melting transitions of the FTIR measurements arises from the lack of a complete unfolded state baseline within the temperature range covered.

3. Cold denatured state of GTT35 The highest transition is within error of the melting temperature of GTT35, 77.4 ± 0.7 °C, determined by circular dichroism and fluorescence thermal melts where guanidine hydrochloride solutions were used to access the unfolded state baseline (Figure S4).[3] This analysis supports the population of at least two thermodynamic states below the main thermal denaturation transition, one of which could be a folding intermediate. Indeed, the 52 °C transition matches the intermediate state at 56 °C in Figure 2, whereas the lowest transition temperature of 16 °C could be due to a cold-denatured state (i.e. an off-pathway state).

While a cold-denatured state of GTT35 has not been previously reported, such a state was previously postulated to exist.[4] WW domains with low melting temperatures have a small region of thermal stability with easily accessible heat and cold denatured states, whereas high melting temperature WW domains like GTT35 have a larger region of thermal stability with cold denaturation reached only at temperatures far below the melting temperature.[4] This analysis is supported by the temperature dependence (Figure S3) of the C3 and C4 spectral components (Figure S2). The C3 spectral component is dominated by a broad positive peak, consistent with disordered structure. A sharp negative peak is overlaid on top of the broad disordered peak, indicating that this component contains a transition from structured to disordered secondary structure. The contribution of the C3 spectral component to the overall spectra increases at low and high temperature (Figure S3), which demonstrates that there is a transition from structured to disordered secondary structure at low and high temperature, consistent with cold and heat denaturation. The C4 spectral component has several sharp features (Figure S2), and the maximum amplitude is reached at ~ 60 °C, with it decaying at high and low temperature as the peptide unfolds (Figure S3). This is consistent with a folded intermediate state or mixture of intermediate states. Differences in amplitude at low and high temperature suggest that there are differences in residual structure of the cold and heat denatured state.

4. The melting temperature of GTT35 was determined by global fitting of circular dichroism and fluorescence thermal melts of FiP35 and GTT35 WW domains where guanidine hydrochloride was used to access the unfolded state baseline. Data was collected in a previous publication,[3] and reanalyzed here. GTT35 is a stabilized variant of FiP35 with a GTT mutation in the second loop. Although both GTT35 and FiP35 are non-two-state folders, a two-state model can be used to approximate the main folding transition. GTT35 has very little unfolded baseline even at the highest guanidine hydrochloride concentration tested. FiP35 and GTT35 have a similar folding cooperativity, so FiP35 and GTT35 data were globally fit to a two-state model (Figure S4):

$$S(T) = [(S_D + m_D T) + (S_N + m_N T)e^{-\Delta G/RT}]/(1 + e^{-\Delta G/RT}) \text{ (S2)},$$

where S_N and S_D are the signal contributions from the native (N) and denatured (D) populations at 0 °C, m_D and m_N are the slope of the native and denatured state baseline and ΔG is the free energy of folding. The free energy of folding is approximated by $\Delta G \approx \Delta G_1(T\text{-}T_m)+\Delta G_2(T\text{-}T_m)^2+\Delta G_D*C$, where C is the guanidine hydrochloride concentration. Circular dichroism and fluorescence thermal melts of FiP35 and GTT35 were simultaneously globally fit to Equation S2, where ΔG parameters (cooperativity parameters ΔG_1, ΔG_2, and ΔG_D) for both proteins were the same for all data sets, FiP35 melts were fit to a single T_m, and GTT35 melts were fit to a single T_m. The signal contributions, S_N and S_D, from the native and denatured populations at 0 °C, and the slopes of the native and denatured state baselines, m_D and m_N, were fixed across the circular dichroism or fluorescence data for each protein (four sets of baselines). Using this method FiP35 fits to a T_m of 72.7 ± 0.2 °C and GTT35 fits to a T_m of 77.3 ± 0.7 °C.

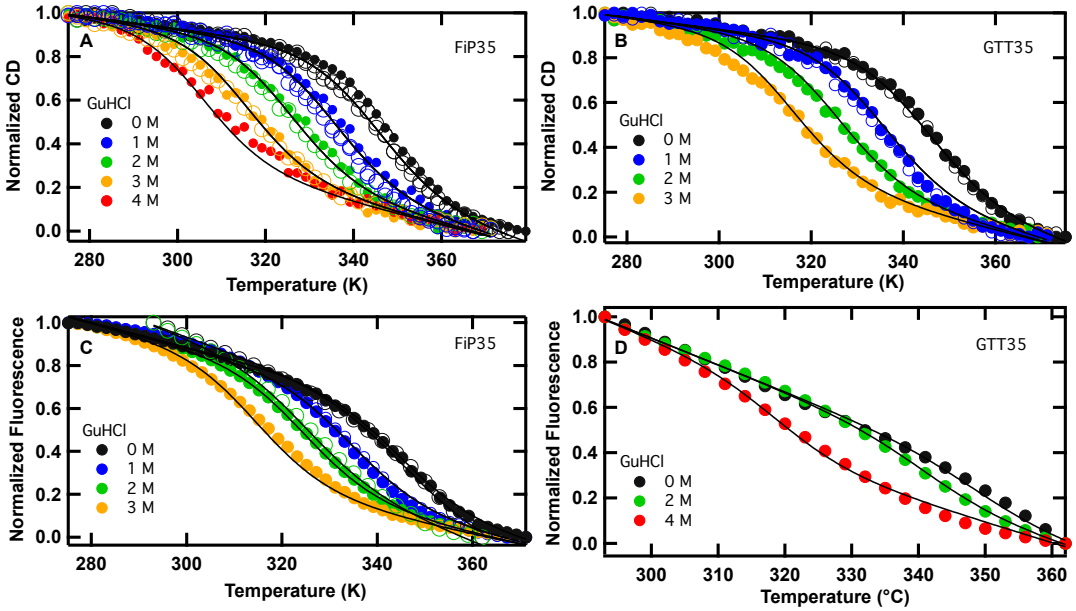

Figure S4. Thermal denaturation of FiP35 (A, C) and GTT35 (B, D) WW domains monitored by circular dichroism (A, B) and fluorescence (C, D). Color indicates the guanidine hydrochloride concentration: 0 M (black), 1 M (blue), 2 M (green), 3 M (orange) or 4 M (red). The continuous lines represent results of a global fit to the data by a two-state model (Equation S2).

5. Arrhenius plots of the observed kinetics reveal the temperature dependence of the three phase of GTT35. The T-jump relaxation methodology is given in the experimental section of the full paper. There are three phases a fast 100's of ns phase, a 1-10 μs phase and a slow 10-100 μs phase. Unlike the slow phase, there is no break at 55 °C in the fast or intermediate phase.

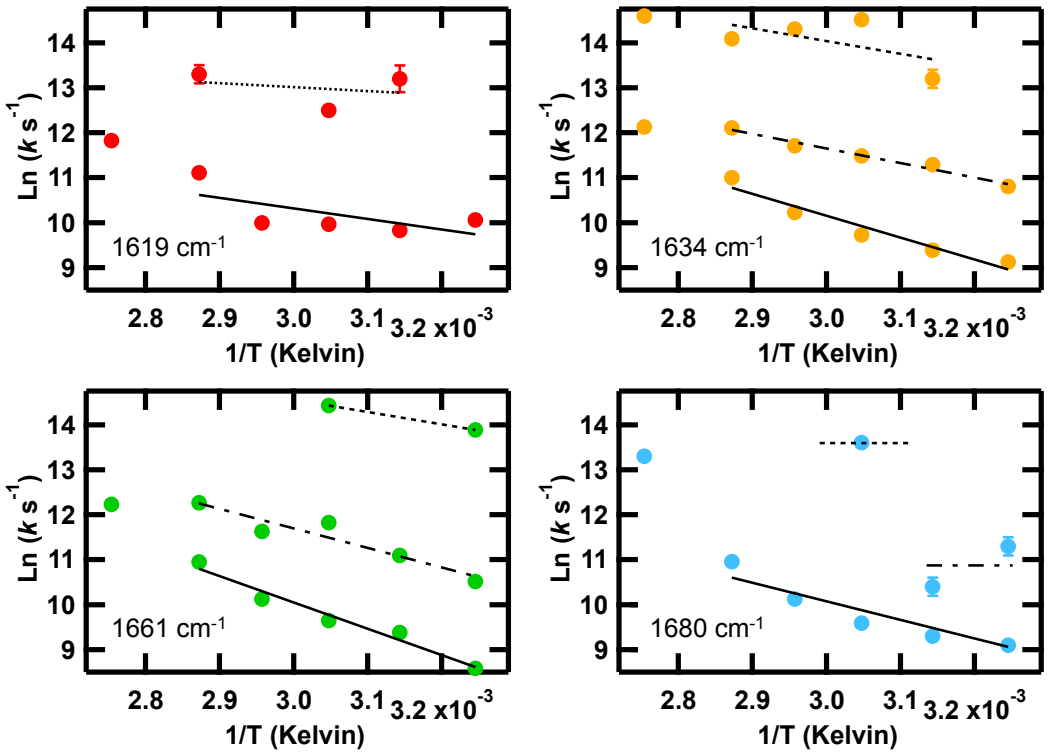

Figure S5. Arrhenius plots showing the temperature dependence of the folding region at 1619 cm^{-1} (red), 1634 cm^{-1} (orange), 1661 cm^{-1} (green), and 1680 cm^{-1} blue. The values of T used for the (1/T) axis are the final temperatures reached during the jump. *k* is the value obtained from a fit (Equation 1) of the T-jump transient. Lines are a result of fitting τ_1 (dotted line), τ_2 (dashed-dot line), and τ_3 (solid line) below T_m. Here the break at 55 °C in the slow phase is neglected.

6. Molecular Dynamics (MD) simulations. The four MD simulations (of lengths 83 μs, 118 μs, 124 μs, and 272 μs; for a total simulation time of ~600 μs) used in the present work were previously performed by the D. E. Shaw Research group on the special-purpose machine Anton.[5] GTT35 was built in an extended conformation and solvated in a cubic box with ~50 side length containing ~4000 TIP3P[6] water molecules and three chlorine ions to achieve a ~30 mM ionic concentration. The simulations were performed using the Amber ff99SB-ILDN force field, which is based on the ff99SB force field[7] with recently improved side-chain torsion parameters.[8] A recent survey of several combinations of force fields and water models assessed the ability of widely used force fields to reproduce experimental data.[9] This survey included the newly developed water model TIP4P-D that improves the description of disordered protein states.[10] The survey showed that for fast-folding peptides, including GTT35, simulations using Amber ff99SB-ILDN/TIP3P show the closest agreement with experimental melting curves, with the caveat that the melting temperatures are overestimated by 10-50 K. All bonds involving hydrogen atoms were constrained to their equilibrium lengths with the SHAKE algorithm.[11] A cutoff of 9.5 for the Lennard-Jones and the short-range electrostatic interactions was used; for the long-range electrostatic interactions the k-Gaussian Split Ewald method was used.[12] The simulations were carried out in the NVT ensemble using the Nose-Hooever thermostat with a relaation time of 1.0 ps saving frames every 200 ps. The simulation temperature was 395 K, a temperature that was previously found to be close to the melting temperature for FiP35 with the force field used.[13] More details on the Molecular Dynamics (MD) simulations can be found in their original works.[3]

7. Definition of GTT conformational states. To investigate the folding kinetics of GTT35 WW domain we defined four conformational states: the folded state (F), the state in which the first hairpin is formed (H1F), the state in which the second hairpin is formed (H2F), and the unfolded state (U). A representative structure of each state is reported in Figure S6. The definition of the H1F and H2F states was motivated by previous experimental and computational studies on other WW domains in general[14] and of FiP35 in particular[15] that reported folding through an intermediate state in which either the first or the second hairpin can fold first. Using the crystal structure of a variant of the Pin1 WW domain with loop 1 shortened (PDB ID: 2F21) as a reference structure for the folded state, the four states were defined using the *R* parameter as a conformational parameter:

$$R = \sum_i \frac{R_i^N}{R_i} \qquad \text{(S3)},$$

where R_i^N is the ith interstrand C_α-C_α distance in two β-hairpins structure in the crystal structure and R_i is the same distance along the four MD simulations. In the first hairpin (H1) there are five interstrand C_α-C_α pairs (W8-N22, E9-F21, K10-Y20, R11-Y19, M12-V18) and in the second hairpin (H2) there are four interstrand C_α-C_α pairs (Y19-W30, Y20-Q29, F21-T28, N22-T27). We thus defined two order parameters on the two hairpins R_{H1} and R_{H2}:

$$R_{H1} = \sum_{i=1}^{4} \frac{R_i^N}{R_i} \qquad \text{(S4)},$$

$$R_{H2} = \sum_{i=1}^{3} \frac{R_i^N}{R_i} \qquad \text{(S5)},$$

neglecting the more external C_α-C_α pair in each hairpin (i.e. the W8-N22 pair in H1 and the Y19-W30 pair in H2) in order to avoid an excessively strict definition of the folded conformation. On the basis of the distribution of R_{H1} and R_{H2} along the MD trajectories we defined the four states as follows:

F state: the nth frame belongs to state F if $R_{H1} \geq 3.8$ and $R_{H2} \geq 2.8$. The population of the F state is 63% along the MD trajectories.

H1F state: the nth frame belongs to state H1F if $R_{H1} \geq 3.8$. The population of the H1F state is 9% along the MD trajectories.

H2F state: the nth frame belongs to state H2F if $R_{H2} \geq 2.8$. The population of the H2F state is 4% along the MD trajectories.

U state: the nth frame belongs to the U state if the frames do not satisfy any of the above criteria. The population of the U state is 24% along the MD trajectories.

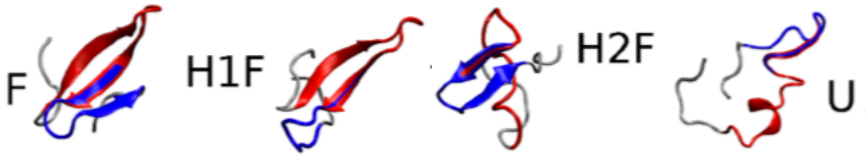

Figure S6. Representative structures of the F, H1F, H2F and U state. In each structure, the residues belonging to hairpin 1 (8-22) are highlighted in red and the ones belonging to hairpin 2 (19-30) are highlighted in blue. Except for the F state, the defined states show a high internal variability, thus the reported structures are just examples of a highly heterogeneous population.

8. Unperturbed Quantum Chemical Calculations Details of the unperturbed quantum chemical calculations were previously described[16] Briefly, quantum chemical calculations were carried out on the isolated trans-NMA molecule at the Time Dependent Density Functional Theory (TDDFT) with the 6-31+G(d) basis set. This level of theory was selected because it represents a good compromise between computational costs and accuracy. The mass-weighted hessian matrix was calculated on the optimized geometry at the B3LYP/6-31+G(d) level of theory and subsequently diagonalized for obtaining the unperturbed eigenvectors and related eigenvalues. The eigenvector corresponding in vacuo to the amide I' mode was then used to generate a grid of points (i.e. configurations) as follows: a step of 0.05 a.u. was adopted and the number of points was set to span an energy range of 20 kJ/mol (in the present case 31 points). For each point, six unperturbed electronic states were then evaluated at the same level of theory providing the basis set for the PMM calculations.

9. Rate constants characterizing the kinetic model The rate constant of U□I, k_1, can be estimated directly from the 24 sub-trajectories by measuring the mean first passage time necessary for each sub-trajectory in state U at t_0=0.8 μs (where stationary state is established) to reach the I state.
From equations 9-12 of the main text and from the estimate of k_1 obtained from the MD simulations (see main text), the remaining rate constants can be obtained:

$$k_{-2} = \frac{k_U k_1}{k_1 - k_F} \qquad \text{(S6)},$$

$$k_2 = \frac{k_F k_{-1}}{k_1 - k_F} \qquad \text{(S7)},$$

$$k_{-1} = \frac{1-\bar{P}_1}{2\bar{P}_1}(k_1 - k_F + k_U) \quad \text{(S8)}.$$

10. Distribution of IR intensities at 1634 cm^{-1}. We applied the MD-PMM methodology to calculate the intensity of the IR signal at the frequency of the maximum peak of the folded-state spectrum (wavenumber=1634 cm^{-1}). The intensity of the IR signal at 1634 cm^{-1} was monitored along the four trajectories: the 4 MD trajectories were divided into segments of 40 ns and, for each segment, the amide I' spectrum was calculated using the corresponding structures. The distribution of the signal obtained at 1634 cm^{-1}, reported in Fig. 7S, is roughly bimodal, confirming that at such a frequency the calculated intensity is sensitive to folded or unfolded structure of the peptide. In fact, in Fig. 7S the distribution calculated on the entire trajectories is compared to the ones calculated on the F and U states only, showing that the low intensity peak essentially corresponds to the U state and the high intensity peak is mainly determined by the F state.

The same intensity distribution was used to select the starting points of the 24 13-μs long subtrajectories. Such initial points were selected among the structures with spectral intensity at 1634 cm^{-1} lying within one standard deviation around the mean of the normal distribution that best fits the low and high intensity band of the whole trajectories intensity distribution for the U and F state, respectively.

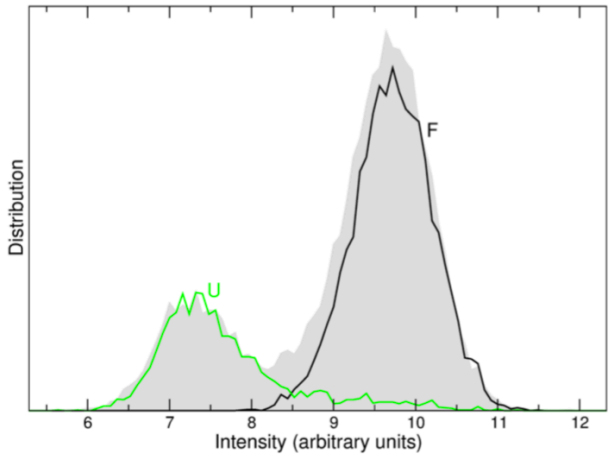

Figure S7. Distribution of IR intensities at wavenumber= 1634 cm^{-1} . The filled gray curve is the distribution of the intensities at 1634 cm^{-1} calculated on the entire 4 MD trajectories, the black and green curves are the same distributions calculated on the folded and unfolded state conformations respectively.

11. Circular Dichroism (CD) measurements were collected to confirm GTT35 WW domain secondary structure. CD wavelength scans and CD melting curves were recorded on a Jasco J-810 spectropolarimeter equipped with a PFD-425S Jasco temperature controller module (Jasco, Inc., Easton, MD). GTT35 was dissolved at 50 μM in 20 mM potassium phosphate buffer pH 7. Wavelength scans were recorded over the range of 260 to 190 nm with an average of 3 repeats. During spectra acquisition, a bandwidth of 2 nm and scan rate of 50 nm/min was used. Thermal unfolding experiments were performed by monitoring the signal at 226 nm from 5 to 95 °C using a 0.1 °C interval and scan rate of 30 °C/hr. During the thermal unfolding experiment a full wavelength scan was obtained every 5 °C after a 60 second delay. The buffer and protein concentrations were the same as used in the wavelength scan experiments.

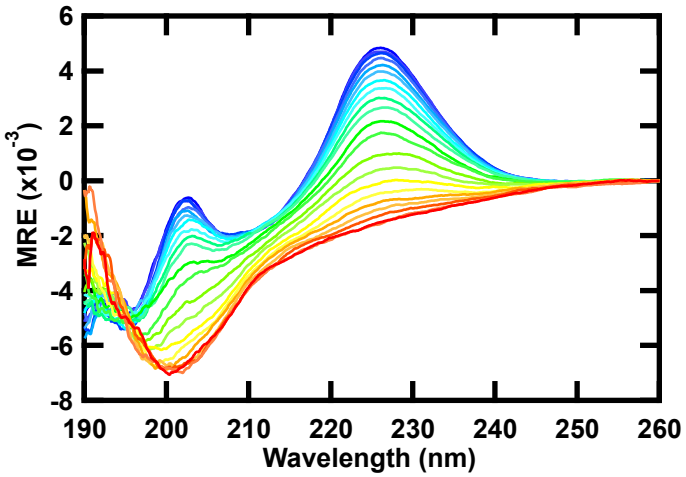

Figure S8. Temperature dependent far-UV CD spectra of 50 μM GTT35 in 20 mM potassium phosphate buffer (pH 7). The temperatures of the individual traces vary from 5 (blue) to 105 °C (red) in 5 °C intervals.

Typically, β-sheet peptides have a CD spectrum with a negative peak at ~218 nm and a positive peak at ~195 nm.[17] WW domains have a unique far-UV CD spectra, dominated by a negative peak at ~202 nm and a positive peak at ~230 nm.[18,19] The peak at ~202 nm resembles the random coil peak usually found at 200 nm. Disorder in the N- and C- termini of the folded structure of WW domains is thought to contribute to this negative peak in the CD spectrum.[19–22] The peak at ~230 nm arises from the presence of ordered aromatic side chains.[17,19,23] Folded Pin1 WW domains and its mutants also have additional structure between 190-210 nm.[24,25] The far-UV CD spectrum of GTT35 WW domain, a Pin1 mutant, is consistent with the Pin1 family WW domain structure (Figure S1). The maximum at 230 nm is an established probe of WW domain structure, which disappears upon unfolding. Thermal denaturation was monitored by recording the ellipticity changes at 226 nm with temperature (Figure S1). GTT35 exhibits typical heat induced unfolding behavior with a loss of intensity at 226 nm and a shift of the minimum at 197 nm to 200 nm, corresponding to a change in secondary structure from folded WW domain to random coil.[19]

12. The magnitude of the T-jump is calculated using the change in reference absorbance with temperature. Equilibrium measurements of the IR absorption of D_2O buffer with no protein as a function of temperature are nearly linear with temperature. As an example, the temperature dependence of the 1619 cm^{-1} absorption of D_2O buffer is reported in Figure S9.

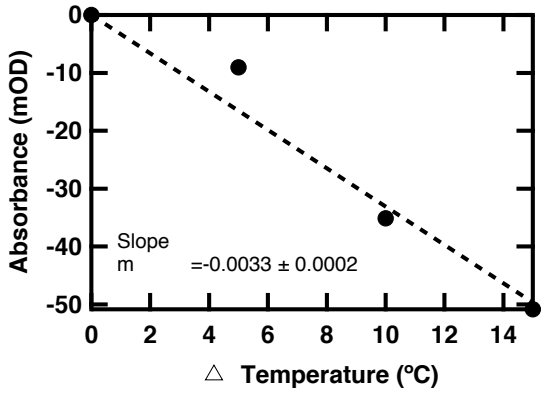

Figure S9. Temperature dependence of D_2O buffer absorbance at 1619 cm^{-1}. The data are fit by a line with the y intercept set to 0.

The IR T-jump relaxation kinetics of D_2O buffer monitored at 1619 cm^{-1} can be used to determine the time dependent temperature change (Figure S10). The absorbance is converted to temperature using the slope (Figure S9) from the equilibrium temperature dependence. The temperature remains constant after the jump from ~7 x 10^{-8} to 5 x 10^{-4} s, the complete window where WW domain kinetics occur.

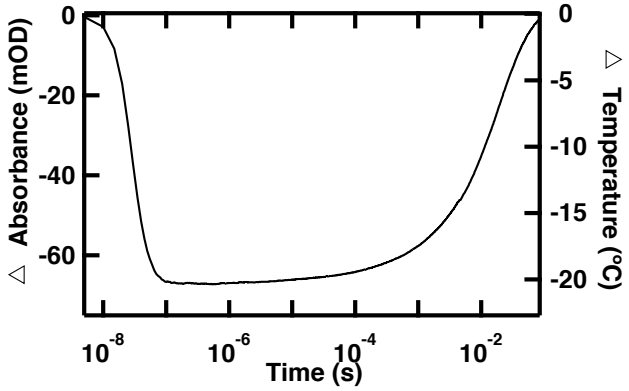

Figure S10. Representative IR T-jump relaxation kinetics of D_2O buffer monitored at 1619 cm^{-1} following a T-jump from 15-35 °C. The change in temperature (right axis) is calculated using the linear temperature dependence of the 1619 cm^{-1} absorption of D_2O buffer (Figure S9).

References

1 R. W. Hendler and R. I. Shrager, *J. Biochem. Biophys. Methods*, 1994, **28**, 1–33.

2 S. H. Brewer, Y. Tang, D. M. Vu, S. Gnanakaran, D. P. Raleigh and R. B. Dyer, *Biochemistry*, 2012, **51**, 5293–5299.

3 S. Piana, K. Sarkar, K. Lindorff-Larsen, M. Guo, M. Gruebele and D. E. Shaw, *J. Mol. Biol.*, 2011, **405**, 43–48.

4 F. Liu, D. Du, A. A. Fuller, J. E. Davoren, P. Wipf, J. W. Kelly and M. Gruebele, *Proc. Natl. Acad. Sci. U. S. A.*, 2008, **105**, 2369–2374.

5 D. E. Shaw, K. J. Bowers, E. Chow, M. P. Eastwood, D. J. Ierardi, J. L. Klepeis, J. S. Kuskin, R. H. Larson, K. Lindorff-Larsen, P. Maragakis, M. A. Moraes, R. O. Dror, S. Piana, Y. Shan, B. Towles, J. K. Salmon, J. P. Grossman, K. M. Mackenzie, J. A. Bank, C. Young, M. M. Deneroff and B. Batson, in *Proceedings of the Conference on High Performance Computing Networking, Storage and Analysis - SC '09*, 2009.

6 W. L. Jorgensen, J. Chandrasekhar, J. D. Madura, R. W. Impey and M. L. Klein, *J. Chem. Phys.*, 1983, **79**, 926–935.

7 V. Hornak, R. Abel, A. Okur, B. Strockbine, A. Roitberg and C. Simmerling, *Proteins Struct. Funct. Genet.*, 2006, **65**, 712–725.

8 K. Lindorff-Larsen, S. Piana, K. Palmo, P. Maragakis, J. L. Klepeis, R. O. Dror and D. E. Shaw, *Proteins Struct. Funct. Bioinforma.*, 2010, **78**, 1950–1958.

9 P. Robustelli, S. Piana and D. E. Shaw, *Proc. Natl. Acad. Sci.*, 2018, 201800690.

10 S. Piana, A. G. Donchev, P. Robustelli and D. E. Shaw, *J. Phys. Chem. B*, 2015, **119**, 5113–5123.

11 R. A. Lippert, K. J. Bowers, R. O. Dror, M. P. Eastwood, B. A. Gregersen, J. L. Klepeis, I. Kolossvary and D. E. Shaw, *J. Chem. Phys.*, 2007, **126**, 046101.

12 Y. Shan, J. L. Klepeis, M. P. Eastwood, R. O. Dror and D. E. Shaw, *J. Chem. Phys.*, 2005, **122**, 54101.

13 D. E. Shaw, P. Maragakis, K. Lindorff-Larsen, S. Piana, R. O. Dror, M. P. Eastwood, J. a Bank, J. M. Jumper, J. K. Salmon, Y. Shan and W. Wriggers, *Science*, 2010, **330**, 341–346.

14 C. M. Davis and R. B. Dyer, *J. Am. Chem. Soc.*, 2016, **138**, 1456–1464.

15 L. Zanetti-Polzi, C. M. Davis, M. Gruebele, R. B. Dyer, A. Amadei and I. Daidone, *FEBS Lett.*, 2017, **591**, 3265–3275.

16 I. Daidone, M. Aschi, L. Zanetti-Polzi, A. Di Nola and A. Amadei, *Chem. Phys. Lett.*, 2010, **488**, 213–218.

17 M. C. Manning and R. W. Woody, *Biopolymers*, 1987, **26**, 1731–1752.

18 E. K. Koepf, H. M. Petrassi, G. Ratnaswamy, M. E. Huff, M. Sudol and J. W. Kelly, *Biochemistry*, 1999, **38**, 14338–14351.

19 E. K. Koepf, H. M. Petrassi, M. Sudol and J. W. Kelly, *Protein Sci.*, 1999, **8**, 841–853.

20 A. R. Viguera, A. Musacchio, M. Saraste, L. Serrano and J. L. R. Arrondo, *Biochemistry*, 1994, **33**, 10925–10933.

21 S. Knapp, P. T. Mattson, P. Christova, K. D. Berndt, A. Karshikoff, M. Vihinen, C. I. E. Smith and R. Ladenstein, *Proteins Struct. Funct. Genet.*, 1998, **31**, 309–319.

22 K. L. Reid, H. M. Rodriguez, B. J. Hillier and L. M. Gregoret, *Protein Sci.*, 1998, **7**, 470–479.

23 N. Ferguson, C. M. Johnson, M. Macias, H. Oschkinat and A. Fersht, *Proc. Natl. Acad. Sci. U. S. A.*, 2001, **98**, 13002–7.

24 M. Jäger, M. Dendle and J. W. Kelly, *Protein Sci.*, 2009, **18**, 1806–1813.

25 M. Jäger, M. Dendle, A. A. Fuller and J. W. Kelly, *Protein Sci.*, 2007, **16**, 2306–2313.

Table 1S: Relaxation kinetics probed in the turn of loop 1 (1619 cm^{-1}) of GTT35 WW domain

T-jump $\Delta T(T_i-T_f)$ °C	A_1 (mOD)	A_2 (mOD)	A_3 (mOD)	τ_1 (µs)	τ_2 (µs)	τ_3 (µs)
20-35			0.67 ± 0.01			42.4 ± 0.7
30-45		0.45 ± 0.01	1.03 ± 0.01		1.9 ± 0.6	54.0 ± 0.7
40-55		0.18 ± 0.01	1.32 ± 0.01		3.8 ± 0.4	46.8 ± 0.7
50-65			1.72 ± 0.01			45.5 ± 0.5
60-75		0.13 ± 0.01	1.48 ± 0.01		1.6 ± 0.3	14.9 ± 0.2
75-90			0.77 ± 0.01			7.3 ± 0.2

Table S2: Relaxation kinetics probed in the β-sheets (1634 cm^{-1}) of GTT35 WW domain

T-jump $\Delta T(T_i-T_f)$ °C	A_1 (mOD)	A_2 (mOD)	A_3 (mOD)	τ_1 (µs)	τ_2 (µs)	τ_3 (µs)
20-35		1.27 ± 0.02	4.08 ± 0.02		20.1 ± 0.4	107.8 ± 0.8
30-45	0.18 ± 0.02	1.46 ± 0.02	8.34 ± 0.02	1.8 ± 0.3	12.5 ± 0.4	83.2 ± 0.3
40-55	0.30 ± 0.01	1.60 ± 0.03	11.29 ± 0.03	0.49 ± 0.04	10.2 ± 0.2	59.2 ± 0.2
50-65	0.50 ± 0.01	2.45 ± 0.04	14.57 ± 0.05	0.61 ± 0.03	8.2 ± 0.2	35.8 ± 0.1
60-75	1.01 ± 0.02	1.5 ± 0.1	11.9 ± 0.1	0.76 ± 0.02	5.5 ± 0.4	16.7 ± 0.1
75-90	0.61 ± 0.04		6.32 ± 0.03	0.45 ± 0.06		5.4 ± 0.5

Table S3: Relaxation kinetics probed in the disordered polypeptide region (1661 cm^{-1}) of GTT35 WW domain

T-jump $\Delta T(T_i-T_f)$ °C	A_1 (mOD)	A_2 (mOD)	A_3 (mOD)	τ_1 (µs)	τ_2 (µs)	τ_3 (µs)
20-35	0.26 ± 0.01	0.70 ± 0.01	0.94 ± 0.01	0.93 ± 0.05	27.0 ± 0.8	186 ± 5
30-45		0.47 ± 0.02	2.10 ± 0.02		15.1 ± 0.7	84 ± 1
40-55	0.31 ± 0.01	0.55 ± 0.01	3.80 ± 0.01	0.54 ± 0.04	7.3 ± 0.3	64.4 ± 0.3
50-65		0.60 ± 0.04	5.23 ± 0.04		8.9 ± 0.6	39.6 ± 0.3
60-75		0.55 ± 0.05	4.77 ± 0.05		4.7 ± 0.4	17.6 ± 0.2
75-90			2.48 ± 0.01			4.90 ± 0.04

Table S4: Relaxation kinetics probed in the β-sheets (1680 cm^{-1}) of GTT35 WW domain

T-jump $\Delta T(T_i-T_f)$ °C	A_1 (mOD)	A_2 (mOD)	A_3 (mOD)	τ_1 (µs)	τ_2 (µs)	τ_3 (µs)
20-35		0.27 ± 0.03	0.40 ± 0.02		26 ± 2	113 ± 7
30-45			1.14 ± 0.01			90.0 ± 0.7
40-55		0.33 ± 0.01	1.49 ± 0.01		1.23 ± 0.05	68.4 ± 0.8
50-65			1.63 ± 0.01			40.0 ± 0.4
60-75			1.19 ± 0.01			17.3 ± 0.1
75-90			0.16 ± 0.01			1.7 ± 0.2